

Massive Dirac surface states in topological insulator/magnetic insulator heterostructures

Weidong Luo¹ and Xiao-Liang Qi²

¹*Geballe Laboratory for Advanced Materials, Stanford University, Stanford, California 94305, USA*

²*Department of Physics, Stanford University, Stanford, California 94305, USA*

(Dated: February 26, 2024)

Topological insulators are new states of matter with a bulk gap and robust gapless surface states protected by time-reversal symmetry. When time-reversal symmetry is broken, the surface states are gapped, which induces a topological response of the system to electromagnetic field—the topological magnetoelectric effect. In this paper we study the behavior of topological surface states in heterostructures formed by a topological insulator and a magnetic insulator. Several magnetic insulators with compatible magnetic structure and relatively good lattice matching with topological insulators Bi_2Se_3 , Bi_2Te_3 , Sb_2Te_3 are identified, and the best candidate material is found to be MnSe , an anti-ferromagnetic insulator. We perform first-principles calculation in $\text{Bi}_2\text{Se}_3/\text{MnSe}$ superlattices and obtain the surface state bandstructure. The magnetic exchange coupling with MnSe induces a gap of ~ 54 meV at the surface states. In addition we tune the distance between Mn ions and TI surface to study the distance dependence of the exchange coupling.

PACS numbers: 73.20.-r, 85.75.-d

Topological insulators (TI) are new states of quantum matter which has the same symmetry as the conventional insulators and semiconductors but cannot be adiabatically deformed to them without going through a phase transition. Recently, time-reversal invariant (TRI) TI's are theoretically predicted and experimentally realized in both two and three dimensions (2D and 3D).¹⁻³ A TRI TI is characterized by robust surface states and unique, quantized response properties, just like the quantized Hall conductance in 2D quantum Hall states. For 3D TI the topological response is the topological magnetoelectric (TME) effect⁴, which is a magneto-electric effect with magnetization \mathbf{M} generated by electric field \mathbf{E} with a quantized coefficient. The TME effect occurs when the surface states of TI become gapped due to time-reversal symmetry breaking, and is a generic property of 3D topological insulators, which can be obtained theoretically from generic models and from an effective field theory approach^{4,5}, independently of microscopic details. Various consequences of the TME effect have been proposed, including Faraday/Kerr rotation of linear polarized light^{4,6-8}, the image monopole effect⁹, the charge carried by a magnetic monopole^{10,11}, and other types of coupling between the charge and spin degree of freedom at the TI surface^{12,13}. Experimental progress has been made recently on the Faraday/Kerr effect in 3D TI¹⁴⁻¹⁷, but the quantized effect predicted have not been observed yet.

To realize the TME effect it is essential to introduce time-reversal symmetry breaking (T-breaking) at the surface of TI to make the surface insulating. There are two possible physical ways to open the T-breaking gap at the surface. The first approach is to introduce magnetic impurities such as Mn or Fe to topological insulators. Both the Dirac-type surface states¹⁸ and the bulk states¹⁹ can mediate ferromagnetic coupling between magnetic impurities and thus induce ferromagnetic order under proper

conditions. The surface state gap induced by doping magnetic impurities Mn and Fe has been observed in various experiments including transport, angle-resolved photo-emission (ARPES) and X-ray magnetic circular dichroism (XMCD)²⁰⁻²². This approach has the advantage of simple experimental setting which can be realized in both bulk materials and thin films. However, the surface state gap is usually small and probably non-uniform due to the low density and disorder effect of the impurities. This may explain why Hall measurements on thin films have observed a large anomalous Hall effect but the longitudinal conductivity is still nonzero.²³ The second approach is to make a heterostructure between a topological insulator and a magnetic insulator (MI), so that the surface states are gapped due to exchange coupling with the MI. Compared to the first approach, this approach has the potential to achieve a stronger and more uniform exchange coupling and thus realize insulating surface states and TME effect in a higher temperature. The main challenge of this approach is to find the suitable material for the MI, which can form a high-quality heterostructure with topological insulators and lead to a strong exchange coupling. This is the goal of the current work.

In this paper we study heterostructures of the Bi_2Se_3 family of TI with MI's. We first carried an extensive material search and identify several materials which have relatively the best lattice matching with TI. The candidate materials are summarized in Table I and their properties will be discussed in more detail in the next section. It is important to notice that some anti-ferromagnetic insulators can also be used to introduce the surface state gap, although a ferromagnetic exchange coupling at the surface is required. Since the exchange coupling is very short-ranged, it will be dominated by the first layer of magnetic ions at the interface of TI and MI. Therefore if an anti-ferromagnetic insulator has magnetic moments

which are aligned to each other in each layer parallel to the surface, but staggering in the perpendicular direction, it provides the same form of ferromagnetic exchange coupling as a ferromagnetic insulator does. In fact, the best candidate material found in our search is an anti-ferromagnetic insulator, MnSe, which is a better candidate than ferromagnetic insulators such as EuS since the latter has magnetism from f -electrons and has a weaker exchange coupling with the p -electrons in TI compared with the d -electrons in MnSe. We present *ab initio* calculation in MnSe/Bi₂Se₃ superlattices, from which we obtain the surface state gap and also describe it in a surface state effective model. In addition we tune the distance between Mn ions and TI surface to study the distance dependence of the exchange coupling. Then we conclude by discussing the band-bending effect caused by the interface charge at the TI/MI junction, which is the main experimental challenge that needs to be addressed in future works.

Criteria and candidate materials

The topological insulators Bi₂Se₃, Bi₂Te₃, and Sb₂Te₃ have layered structure, and the 2-dimensional lattice within each layer has triangular symmetry. The 2D lattice constants of Bi₂Se₃, Bi₂Te₃, and Sb₂Te₃ are 4.1355 Å²⁴, 4.395 Å²⁵, and 4.264 Å²⁶, respectively. We look for candidate MI materials with 2D crystal plane of compatible symmetry to TI layers, ie. hexagonal lattice. The other criteria for the candidate MI materials include similar lattice constant, and ferromagnetic moments in the 2D hexagonal interface atomic plane.

A list of candidate MI materials is shown in table I. EuO²⁷, EuS²⁸, EuSe²⁹, and MnSe³⁰ have the cubic rock-salt structure, of which the atoms in the (111) plane form triangular lattice, with compatible lattice constant to the TIs. Both EuO and EuS are ferromagnetic insulators, which meets the requirement of correct magnetic configuration, however the lattice constant of EuO is too small for good lattice matching with the common 3D topological insulators. EuSe has a complex magnetic phase diagram, and it also becomes FM under suitable pressure range. Magnetism in EuO, EuS and EuSe originates from the half-filled $4f$ orbitals of the Eu⁺² ions. MnSe has the type-II (G-type) anti-ferromagnetic structure, of which the magnetic moments in each (111) atomic planes are ferromagnetic. MnTe³¹ is chemically similar to MnSe, although it has a hexagonal lattice. Mn moments in MnTe also have an AFM configuration, formed of alternating hexagonal (0001) FM planes. Magnetism in MnSe and MnTe comes from the high-spin d^5 orbitals of the Mn⁺² ions. RbMnCl₃³² is also in hexagonal structure, with the Mn sites forming alternating (0001) FM planes. Although its hexagonal plane has a much larger lattice constant, it matches the $\sqrt{3} \times \sqrt{3}$ reconstruction of the in-plane lattice of Bi₂Se₃. Thus RbMnCl₃ is a potential candidate material, although the magnetic coupling would be weaker because only 1/3 of the atomic sites of the TIs will be in contact with the Mn sites.

In the candidate materials listed in Table I, we

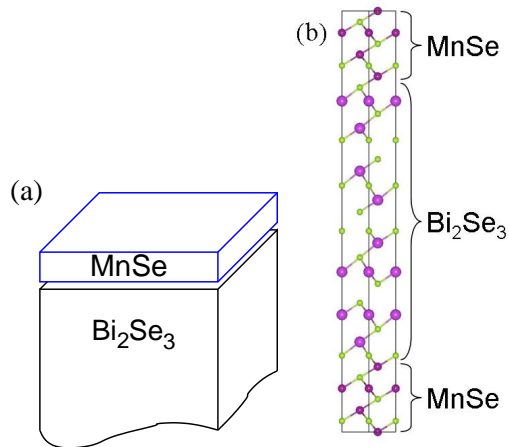


FIG. 1: (color online). (a) Schematic picture of a MnSe film deposited on the surface of Bi₂Se₃. (b) Crystal structure of the supercell structure in the first-principles calculations.

carried *ab initio* calculations to several of them including MnSe/Bi₂Se₃, MnTe/Bi₂Se₃, MnTe/Sb₂Te₃, EuS/Bi₂Se₃ and EuSe/Bi₂Se₃. Among these heterostructures, we find MnSe/Bi₂Se₃ to be the best one, with relatively strong exchange-coupling and simple surface state band structure. In the following we will focus on the results of MnSe/Bi₂Se₃ heterostructure, and present the results on MnTe/Sb₂Te₃ and MnTe/Bi₂Se₃ in the appendix as a comparison.

Bi₂Se₃/MnSe interface

We study the Bi₂Se₃/MnSe interface by constructing a superlattice composed of Bi₂Se₃ slab and MnSe slab. The supercells employed in the first-principles calculations are required to have inversion symmetry, and the Mn atoms at the top and bottom surfaces of Bi₂Se₃ slab have parallel spin orientation. The thickness of the Bi₂Se₃ slab is chosen to be 4 QLs, the MnSe slab is determined to have a thickness of $6n+1$ (7, 13, 19, ...) layers, in order to meet the requirements of inversion symmetry and parallel spin orientations. To simulate the physical system of a MnSe film deposited on top of a bulk Bi₂Se₃, the in-plane lattice constant of the MnSe is fixed to that of Bi₂Se₃, and the out-of-plane lattice constant is determined by energy optimization. The 4-7 supercell structure (composed of 4 QLs of Bi₂Se₃ and 7 layers of MnSe) is shown in fig. 1(b).

First-principles density functional theory (DFT) calculations are performed to optimize the supercell structure and to obtain the electronic band structure. We used the Hohenberg-Kohn density-functional theory with the generalized-gradient approximation (GGA)³³ and the projector augmented-wave method as implemented in VASP³⁴⁻³⁶. The Mn $3d$ orbitals are treated with the GGA plus Hubbard U (GGA+ U) method^{37,38}, and typical values of correlation parameters are used^{39,40}: $U = 5.0$ eV, and $J = 1.0$ eV.

If not noted otherwise (as when tuning the separation distance between Bi₂Se₃ and MnSe slabs), the atomic

TABLE I: A list of candidate magnetic insulators and their properties.

Materials	Structure	Lattice matching	Magnetic phase	Comments
EuO	rocksalt, $a = 5.145 \text{ \AA}$	$5.145/\sqrt{2}$ $= 3.64 \text{ \AA}$	FM	4f electrons weak coupling
EuS	rocksalt, $a = 5.98 \text{ \AA}$	$5.98/\sqrt{2}$ $= 4.23 \text{ \AA}$	FM	4f electrons weak coupling
EuSe	rocksalt, $a = 6.192 \text{ \AA}$	$6.192/\sqrt{2}$ $= 4.38 \text{ \AA}$	complex, FM under P	4f electrons weak coupling
MnSe	rocksalt, $a = 5.464 \text{ \AA}$	$5.464/\sqrt{2}$ $= 3.86 \text{ \AA}$	type-II AFM, FM (111) planes	3d electrons stronger coupling
MnTe	hexagonal, $a = 4.1497 \text{ \AA}$	4.1497 \AA	AFM, FM (0001) planes	3d electrons stronger coupling
RbMnCl ₃	hexagonal, $a = 7.16 \text{ \AA}$	$7.16/\sqrt{3}$ $= 4.13 \text{ \AA}$	AFM, FM (0001) planes	only 1/3 of lattice points

coordinates of the superlattice are optimized as in the following. The middle part of the Bi₂Se₃ slab is fixed to the experimental structure, while the atomic coordinates of the whole MnSe slab together with the first Bi and Se atomic planes of Bi₂Se₃ at the interface are optimized according to the forces from first-principles calculations. *Bandstructure.*— We first investigate the 4-13 Bi₂Se₃/MnSe superlattice, with Mn spins along [001] direction. The bandstructure from first-principles calculations is shown in fig. 2. By projecting the bands to the Bi and Se atoms of the top and bottom surfaces, shown in fig. 2(a), we identify the Dirac cone feature located about 0.4 eV below the bulk gap of Bi₂Se₃ as surface states of Bi₂Se₃. Further analysis on the spin directions of the states around Γ point confirms it to be the topological surface state. A small gap appears at the Dirac point, and both the lower and upper Dirac cones

show spin related energy splitting in the vicinity of Γ point, indicating the magnetic interaction with MnSe.

The band gap of MnSe is much larger than that of Bi₂Se₃. In order to obtain a clearer picture of the electronic states of the two materials forming the superlattice, we project the bands separately to the Bi₂Se₃ slab and the MnSe slab in the superlattice, shown in fig. 2(b). The bulk gap of Bi₂Se₃, as well as the Dirac cone states, are located in the band gap of MnSe, which makes it possible to realize a fully gapped system and observe the TME effect.

Effective model fitting.— To gain better understanding of the exchange coupling experienced by the surface states, we introduce an effective Hamiltonian H_{eff} for the Dirac fermion surface states of the topological insulator thin film coupled with the exchange field⁴¹

$$H_{\text{eff}} = Dk^2I + \begin{pmatrix} \hbar v_F(\sigma_x k_y - \sigma_y k_x) + \mathbf{M} \cdot \boldsymbol{\sigma} & tI \\ tI & -\hbar v_F(\sigma_x k_y - \sigma_y k_x) + \mathbf{M} \cdot \boldsymbol{\sigma} \end{pmatrix}, \quad (1)$$

Here σ_i ($i = x, y, z$) are the Pauli matrices, and I the identity matrix. \mathbf{M} and t correspond to the effective magnetic field acting on the Dirac fermion surface states and the inter-edge interaction between the two surfaces. The other parameters in the model are: D , the quadratic term, and v_F the Fermi velocity.

The eigen-energies of the model Hamiltonian can be solved analytically,

$$E = Dk^2 \pm \sqrt{k^2 + M^2 + t^2 \pm 2\sqrt{M^2 t^2 + (M_x k_y - M_y k_x)^2}}, \quad (2)$$

here we set $\hbar v_F = 1$. We note that at Γ point ($k = 0$),

the four eigen-energies are $E = \pm(M \pm t)$. In the case of strong magnetic coupling and weak inter-edge interaction where $M > t$, the zone-center eigen-energies (from low energy to high energy) and the corresponding spin orientations are: $-M - t$ (spin down), $-M + t$ (spin down), $M - t$ (spin up), and $M + t$ (spin up). In the opposite case where $M < t$, the zone-center eigen-energies and spin orientations are: $-M - t$ (spin down), $M - t$ (spin up), $-M + t$ (spin down), and $M + t$ (spin up). In both cases, an energy gap Δ forms at the original Dirac point, $\Delta = 2|M - t|$.

The Dirac fermion bandstructure obtained from first-principles calculations is fitted to the model solution in

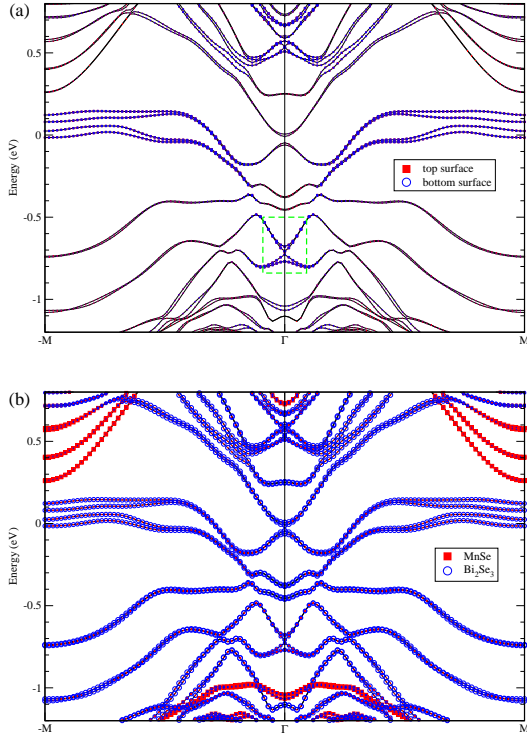


FIG. 2: (color online). Bandstructure of the $\text{Bi}_2\text{Se}_3/\text{MnTe}$ superlattice. The two panels show the projection of the wavefunctions to the Bi and Se atoms at the top and bottom surfaces (a), and that to the two materials Bi_2Se_3 and MnSe (b). The calculation is done for the superlattice structure composed of 4 quintuple layers of Bi_2Se_3 and 13 layers of MnSe, with Mn spins along $[001]$ direction.

equation 2. For the superlattice structure composed of 4 quintuple layers of Bi_2Se_3 and 13 layers of MnSe with Mn spins along $[001]$ direction, the calculated Dirac fermion surface states around Γ point for crystal momentum along k_x (Γ -M) direction are fitted satisfactorily to the model solution, as shown in figure 3(a). The fitting parameters are: $M = 28.2$ meV, $t = 17.6$ meV, $D = 9.8$ eV \AA^2 , and $v_F = 2.66 \times 10^5$ m/s. Fitting the model solution to the calculated band dispersion along k_y (Γ -K) direction results in very similar parameters, $D = 9.9$ eV \AA^2 , and $v_F = 2.70 \times 10^5$ m/s.

Distance dependence of parameters t and M .— To understand the behavior of large physical system, we investigate the dependence of the effective magnetic field M and inter-edge interaction t on the thickness of the MnSe slab in the superlattice structure. First-principles band structure calculations of the 4-7 (composed of 4 QLs of Bi_2Se_3 and 7 layers of MnSe), 4-13, and 4-19 $\text{Bi}_2\text{Se}_3/\text{MnSe}$ superlattices were fitted to the model solution using equation 2. The fitting parameters M and t are plotted as a function of the MnSe layer number, as shown in fig. 3(b). The effective magnetic field M does not vary strongly as the number of MnSe layers increases, consistent with the fact that it is mostly due to the magnetic exchange coupling between the MnSe

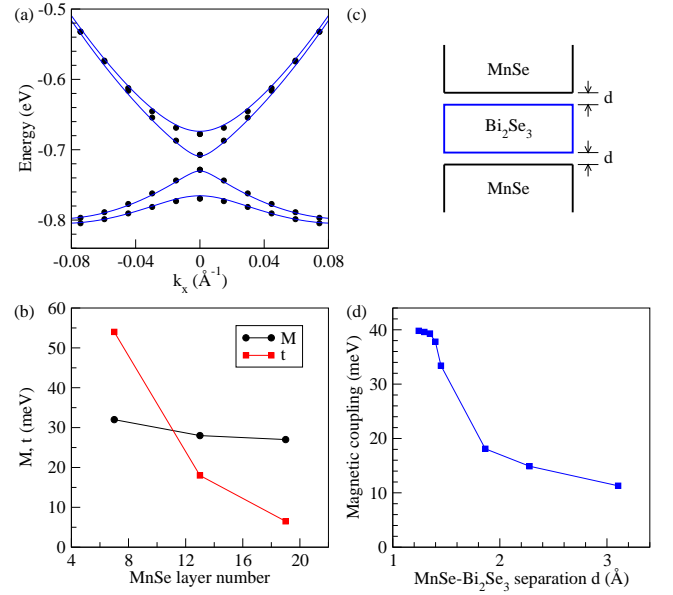


FIG. 3: (color online). (a) The calculated band structure (black circle, the same data as Fig. 2) is fitted by the effective model (1) (blue curves). (b) The dependence of the inter-edge interaction t and the effective exchange field M on the thickness of the MnSe slab, obtained from the fitting. (c) A schematic picture of the material structure used in the calculations shown in the next panel, with the distance d between MnSe and Bi_2Se_3 tuned (see text). (d) Dependence of M on the separation d between the Bi_2Se_3 and MnSe slabs.

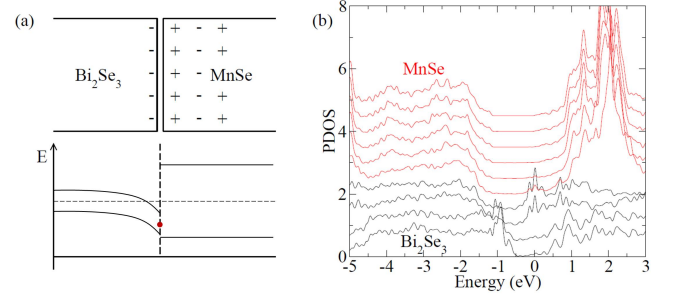


FIG. 4: (color online). (a) Illustration of the charge states at the $\text{Bi}_2\text{Se}_3/\text{MnSe}$ interface, and a schematic picture of band bending, where the (red) dot at the interface represents the surface state Dirac point. (b) The calculated projected density-of-states of Bi_2Se_3 (black) and MnSe (red) for lattice sites across the surface, showing the band bending at the interface. Here each curve for MnSe represents one MnSe bilayer, and each curve for Bi_2Se_3 represents one BiSe bilayer in either the top or bottom half of the quintuple layers.

and the surface states of Bi_2Se_3 at the interface. In contrast, the inter-edge interaction t decreases rapidly as the number of MnSe layers increases. This indicates that the inter-edge interaction in smaller superlattices are mediated mostly through the MnSe slab, instead of within the Bi_2Se_3 layers. The strong effective magnetic field ($M \sim 27$ meV) at this interface results in a large gap open-

ing ($2M \sim 54$ meV) in realistic experimental setup with thicker MnSe slab, which holds promise for magnetic manipulation of TI surface states at room temperature.

In our calculation a perfect interface between MnSe and Bi_2Se_3 is assumed. In reality, the interface will probably contain impurities and defects, so that the coupling between Mn and Se across the surface is weaker. To see how the magnetic exchange coupling is affected by the distance between Mn and Se atoms, we now keep fixed the atomic coordinates within the Bi_2Se_3 and MnSe slabs, but varying the separation d between the Bi_2Se_3 and MnSe slabs, as shown in fig. 3(c). As the effective magnetic field M is mostly due to the exchange coupling between MnSe and Bi_2Se_3 across the interface, we expect a strong dependence of M on the separation distance d . For the 4-13 $\text{Bi}_2\text{Se}_3/\text{MnSe}$ superlattice, the effective magnetic field M is plotted in fig. 3(d), showing a strong dependence of M as a function of the separation d between Bi_2Se_3 and MnSe. This result indicates that the magnetic exchange coupling at the TI-MI interface could be tuned by applying external pressure.

Surface charge and band bending

Although the Dirac cone is in the bulk gap of MnSe, from the band structure shown in Fig. 2 we see some additional hole-type bands coexisting with the massive Dirac cone. These bands can be understood as a consequence of the band bending occurring at the heterostructure. Band bending at a heterojunction is common. In MnSe, Mn^{2+} and Se^{2-} ions carry positive and negative charge, respectively. Consequently, the Mn terminated surface considered here carries a finite positive charge density. Since the Bi_2Se_3 is a covalent material and has no surface charge, the net charge of the heterojunction

between these two materials is positive, leading to a trap for the surface electrons. Therefore the bands bend down around the interface, as is illustrated in Fig. 4(a). leading to the additional surface state bands.

We studied the band bending effect by calculating the electronic density-of-states projected to individual atomic planes. The projected density-of-states (PDOS) of the Mn-Se atomic planes are shown in red curves in fig. 4(b), while the PDOS for the top and bottom Bi-Se atomic planes in the Bi_2Se_3 slab are shown in black curves. It is clear that very little band bending exists in MnSe, while there is significant shift between the states of the first and second QLs in Bi_2Se_3 . The electronic states in the first QL of Bi_2Se_3 is shifted down in energy compared to the second QL, consistent with the direction of the interface electric dipole moment shown in fig. 4(a).

The additional surface states lead to difficulty in opening a full gap at the surface, the solution of which is the main open question we leave for future theoretical and experimental works. Possible solutions include screening the surface charge by a top gate, or by proper chemical doping at the junction.

Acknowledgements

We acknowledge helpful discussions with Haijun Zhang and Shou-Cheng Zhang. This work is supported by the Defense Advanced Research Projects Agency Microsystems Technology Office, MesoDynamic Architecture Program (MESO) through the contract number N66001-11-1-4105. Computations were performed at the National Energy Research Scientific Computing Center (NERSC), which is supported by the Office of Science of the U.S. Department of Energy under Contract No. DE-AC02-05CH11231.

-
- ¹ J. E. Moore, Nature **464**, 194 (2010).
 - ² M. Z. Hasan and C. L. Kane, Rev. Mod. Phys. **82**, 3045 (2010).
 - ³ X.-L. Qi and S.-C. Zhang, Rev. Mod. Phys. **83**, 1057 (2011).
 - ⁴ X.-L. Qi, T. Hughes, and S.-C. Zhang, Phys. Rev. B **78**, 195424 (2008).
 - ⁵ A. M. Essin, J. E. Moore, and D. Vanderbilt, Phys. Rev. Lett. **102**, 146805 (2009).
 - ⁶ A. Karch, Phys. Rev. Lett. **103**, 171601 (2009).
 - ⁷ J. Maciejko, X.-L. Qi, H. D. Drew, and S.-C. Zhang, Phys. Rev. Lett. **105**, 166803 (2010).
 - ⁸ A. H. M. Wang-Kong Tse, Phys. Rev. Lett. **105**, 057401 (2010).
 - ⁹ X.-L. Qi, R. Li, J. Zang, and S.-C. Zhang, Science **323**, 1184 (2009).
 - ¹⁰ G. Rosenberg and M. Franz, Phys. Rev. B **82**, 035105 (2010).
 - ¹¹ G. Rosenberg, H.-M. Guo, and M. Franz, Phys. Rev. B **82**, 041104 (2010).
 - ¹² T. Yokoyama, J. Zang, and N. Nagaosa, Phys. Rev. B **81**, 241410 (2010).
 - ¹³ K. Nomura and N. Nagaosa, Phys. Rev. B **82**, 161401(R) (2010).
 - ¹⁴ R. V. Aguilar, A. Stier, W. Liu, L. Bilbro, D. George, N. Bansal, J. Cerne, A. Markelz, S. Oh, and N. Armitage, *Thz response and colossal magneto-electric effect in the topological insulator bi_2se_3* , e-print arXiv:1105.0237 (2011).
 - ¹⁵ A. D. LaForge, A. Frenzel, B. C. Pursley, T. Lin, X. Liu, J. Shi, and D. N. Basov, Phys. Rev. B **81**, 125120 (2010).
 - ¹⁶ A. B. Sushkov, G. S. Jenkins, D. C. Schmadel, N. P. Butch, J. Paglione, and H. D. Drew, Phys. Rev. B **82**, 125110 (2010).
 - ¹⁷ G. S. Jenkins, A. B. Sushkov, D. C. Schmadel, N. P. Butch, P. Syers, J. Paglione, and H. D. Drew, Phys. Rev. B **82**, 125120 (2010).
 - ¹⁸ Q. Liu, C.-X. Liu, C. Xu, X.-L. Qi, and S.-C. Zhang, Phys. Rev. Lett. **102**, 156603 (2009).
 - ¹⁹ R. Yu, W. Zhang, H. J. Zhang, S. C. Zhang, X. Dai, and Z. Fang, Science **329**, 61 (2010).
 - ²⁰ Y. L. Chen, J.-H. Chu, J. G. Analytis, Z. K. Liu, K. Igarashi, H.-H. Kuo, X. L. Qi, S. K. Mo, R. G. Moore, D. H. Lu, et al., Science **329**, 659 (2010).
 - ²¹ S.-Y. Xu, M. Neupane, C. Liu, D. M. Zhang, A. Richardella, L. A. Wray, N. Alidoust, M. Leandersson, T. Balasubramanian, J. Sanchez-Barriga, et al., *Mag-*

- netically induced spin reorientation and magnetic transition on the surface of a topological insulator*, e-print arXiv:1206.2090.
- ²² M. Liu, J. Zhang, C.-Z. Chang, Z. Zhang, X. Feng, K. Li, K. He, L.-l. Wang, X. Chen, X. Dai, et al., Phys. Rev. Lett. **108**, 036805 (2012), URL <http://link.aps.org/doi/10.1103/PhysRevLett.108.036805>.
 - ²³ C.-Z. Chang, J.-S. Zhang, M.-H. Liu, Z.-C. Zhang, X. Feng, K. Li, L.-L. Wang, X. Chen, X. Dai, Z. Fang, et al., *Carrier-independent ferromagnetism and giant anomalous hall effect in magnetic topological insulator*, e-print arXiv:1108.4754 (2011).
 - ²⁴ C. Pérez Vicente, J. L. Tirado, K. Adouby, J. C. Jumas, A. Abba Touré, and G. Kra, Inorg. Chem. **38**, 2131 (1999).
 - ²⁵ Y. Feutelais, B. Legendre, N. Rodier, and V. Agafonov, Mater. Res. Bull. **28**, 591 (1993).
 - ²⁶ T. L. Anderson and H. B. Krause, Acta Cryst. **B30**, 1307 (1974).
 - ²⁷ D. B. McWhan, P. C. Souers, and G. Jura, Phys. Rev. **143**, 385 (1966).
 - ²⁸ M. Palazii and E. Bretey, Mater. Res. Bull. **24**, 695 (1989).
 - ²⁹ K. Westerholt and H. Bach, Phys. Rev. B **31**, 7151 (1985).
 - ³⁰ A. J. Jacobson and B. E. F. Fender, J. Chem. Phys. **52**, 4563 (1970).
 - ³¹ S. S. A. Noor, J. Appl. Phys. **61**, 3549 (1987).
 - ³² E. M. Ali and A. A. Felimban, Aust. J. Phys. **42**, 307 (1989).
 - ³³ J. P. Perdew, K. Burke, and M. Ernzerhof, Phys. Rev. Lett. **77**, 3865 (1996).
 - ³⁴ P. E. Blöchl, Phys. Rev. B **50**, 17953 (1994).
 - ³⁵ G. Kresse and J. Furthmüller, Phys. Rev. B **54**, 11169 (1996).
 - ³⁶ G. Kresse and D. Joubert, Phys. Rev. B **59**, 1758 (1999).
 - ³⁷ V. I. Anisimov, J. Zaanen, and O. K. Andersen, Phys. Rev. B **44**, 943 (1991).
 - ³⁸ A. I. Liechtenstein, V. I. Anisimov, and J. Zaanen, Phys. Rev. B **52**, R5467 (1995).
 - ³⁹ S. J. Youn, Journal of Magnetism **10**, 71 (2005).
 - ⁴⁰ P. Amiri, S. J. Hashemifar, and H. Akbarzadeh, Phys. Rev. B **83**, 165424 (2011).
 - ⁴¹ C.-X. Liu, X.-L. Qi, H. Zhang, X. Dai, Z. Fang, and S.-C. Zhang, Phys. Rev. B **82**, 045122 (2010).

Appendix A: In-plane magnetization

As a comparison, we also calculated the bandstructure of $\text{Bi}_2\text{Se}_3/\text{MnSe}$ superlattice with Mn spins along the in-plane $[100]$ direction. The bandstructure along k_y (Γ -K) direction with projection of the bands to the Bi and Se atoms of the top and bottom surfaces is shown in fig. 5(a). Similar to the case of $[001]$ spin orientation shown in Fig. 2, the Dirac-cone states are located about 0.4 eV below the bulk gap of Bi_2Se_3 . One prominent feature is that the Dirac-cone states of the top and bottom surfaces are shifted to opposite directions along k_y axis. For a Fermi energy above the Dirac cone, the Fermi surfaces from the top and bottom surfaces of Bi_2Se_3 will shift to opposite directions in the momentum space. Fig. 5(b) illustrates the opposite shift of the two Fermi surfaces along k_y direction, and the corresponding spin directions.

By fitting the effective model (1) with an in-plane exchange field, we have extracted the exchange coupling M and inter-edge interaction t . For the 4-13 superlattice structure with in-plane magnetization, we obtain $M = 9$ meV, and $t = 19$ meV. The value of t mostly depends on the thickness of MnSe and Bi_2Se_3 slabs, so t in the case of in-plane magnetization is similar to the value for perpendicular magnetization. However the exchange coupling is quite anisotropic, and it is much smaller in the case of in-plane magnetization compared to the perpendicular one.

Appendix B: $\text{Sb}_2\text{Te}_3/\text{MnTe}$ interface

Other materials in our study include the $\text{Sb}_2\text{Te}_3/\text{MnTe}$ heterostructure. The calculated bandstructure of the 4-13 superlattice with projection of the bands to the Sb and Te atoms at the top and bottom surfaces is shown in fig. 6(a). In contrast to the $\text{Bi}_2\text{Se}_3/\text{MnSe}$ heterostructure, there is complicated hybridization of bulk and surface states in the $\text{Sb}_2\text{Te}_3/\text{MnTe}$ heterostructure, and the Dirac-cone feature can not be easily identified.

We project the bands separately to the Sb_2Te_3 slab and the MnTe slab in the superlattice, as shown in fig. 6(b). Although the bulk band gap of MnTe at Γ point is much larger than Sb_2Te_3 , the bulk band gap of Sb_2Te_3 is located close in energy to the top of valence band of MnTe, and the Dirac surface states overlap in energy with the valence band of MnTe. Therefore it is less likely to realize a fully gapped system in $\text{Sb}_2\text{Te}_3/\text{MnTe}$ heterostructure.

Appendix C: $\text{Bi}_2\text{Se}_3/\text{MnTe}$ interface

We have also studied the $\text{Bi}_2\text{Se}_3/\text{MnTe}$ heterostructure with supercell composed of 4 QLs of Bi_2Se_3 and 7 layers of MnTe. The calculated bandstructure with projection of the bands to the Bi and Se atoms at the top and bottom

surfaces is shown in fig. 7. Similar to the $\text{Sb}_2\text{Te}_3/\text{MnTe}$ heterostructure, the surface states and bulk states in the $\text{Bi}_2\text{Se}_3/\text{MnTe}$ heterostructure are also strongly hybridized, and the Dirac-cone feature can not be easily identified.

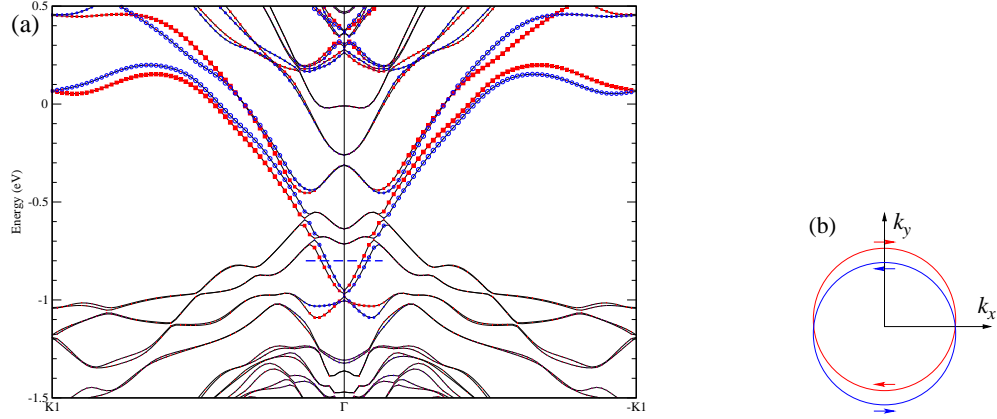


FIG. 5: (Color online) (a) Bandstructure of the $\text{Bi}_2\text{Se}_3/\text{MnSe}$ superlattice along k_y (Γ -K) direction. The red and blue symbols show the projection of the wavefunctions to the Bi and Se atoms at the top and bottom surfaces. (b) a schematic showing the Fermi surfaces of n -doped surface states at the two surfaces of Bi_2Se_3 . The Fermi energy is taken at the dashed line in (a). The calculation is performed for superlattice structure composed of 4 QLs of Bi_2Se_3 and 13 layers of MnSe , with Mn spins along $[100]$ direction.

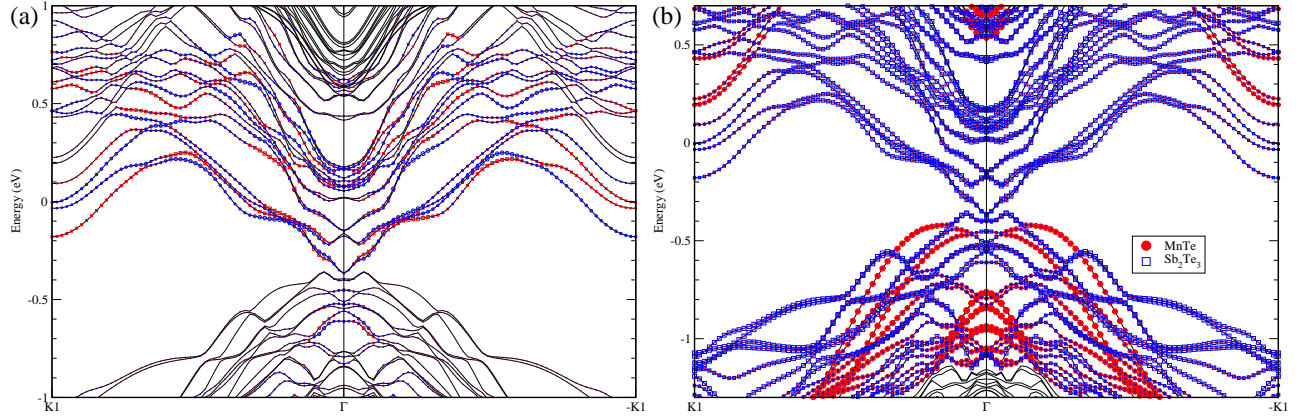


FIG. 6: (Color online) Bandstructure of the $\text{Sb}_2\text{Te}_3/\text{MnTe}$ superlattice. The two panels show the projection of the wavefunctions to the Sb and Te atoms at the top (red symbols) and bottom (blue symbols) surfaces (a), and that to the two materials Sb_2Te_3 and MnTe (b). The calculation is done for the superlattice structure composed of 4 QLs of Sb_2Te_3 and 13 layers of MnTe , with Mn spins along $[001]$ direction.

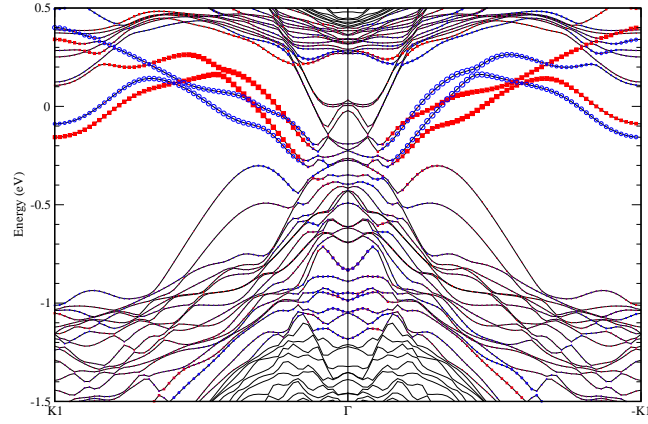


FIG. 7: (Color online) Bandstructure of the $\text{Bi}_2\text{Se}_3/\text{MnTe}$ superlattice, showing the projection of the wavefunctions to the Bi and Se atoms at the top (red symbols) and bottom (blue symbols) surfaces. The calculation is done for the superlattice structure composed of 4 QLs of Bi_2Se_3 and 7 layers of MnTe, with Mn spins along $[001]$ direction.